

Temperature tunability in $\text{Sr}_{1-x}\text{Ca}_x\text{FeO}_{3-\delta}$ for reversible oxygen storage: a computational and experimental study

Eric J. Popczun^{ab}, De Nyago Tafen^{ac}, Sittichai Natesakhawat^{ad}, Chris M. Marin^{ab}, Thuy-Duong Nguyen-Phan^{ab}, Yunyun Zhou^a, Dominic Alfonso^a and Jonathan W. Lekse^{*a}

^aNational Energy Technology Laboratory, 626 Cochrans Mill Rd, Pittsburgh, PA 15236, USA.

^bLeidos Research Support Team, 626 Cochrans Mill Rd, Pittsburgh, PA 15236, USA

^cLeidos Research Support Team, 1450 Queen Avenue SW, Albany, OR 97321, USA

^dDepartment of Chemical and Petroleum Engineering, University of Pittsburgh, Pittsburgh, PA 15260, USA

Abstract

Reversible oxygen absorption/desorption in earth-abundant materials is fundamental towards many advanced technologies that require a pure oxygen stream including oxy-combustion via chemical looping and oxygen-blown coal gasification. The $\text{Sr}_{1-x}\text{Ca}_x\text{FeO}_3$ system is one of many perovskite oxides that have drawn attention given the large quantities of oxygen it can produce during mild cycling conditions. In this work, we employ hybrid functional based DFT calculations to establish the oxygen vacancy formation energy, $\Delta E_{f,\text{vac}}$, as an effective parameter for describing the $\text{Sr}_{1-x}\text{Ca}_x\text{FeO}_3$ system. We validate these calculations experimentally using XPS, O_2 -TPD, TGA, and synchrotron pXRD. In all cases, we find that increasing calcium content lowers both the oxygen desorption temperature and preferred operating temperature for the system. Importantly, we are able to experimentally show the structural and functional cyclability of these materials, achieving rapidly accessible maximum oxygen storage capacities of 1.51–2.41 wt% for temperatures of 400–700 °C.

Introduction

Development for new oxygen storage materials has become increasingly vital over the past few decades given the emergence of many technologies including chemical looping combustion,¹ syngas production,^{2,3} solid oxide fuel cells,^{4,5} three-way catalysis,^{1,2,6} and oxygen sensors.^{7,8} An Air Separation Unit (ASU) is fundamental in a new pilot natural gas power plant design developed by NET Power. By including an ASU, many common impurities can be removed from the combustion atmosphere leading to clean CO_2 production, which would eliminate the need for expensive carbon capture.⁹ For this developing technology, as well as the others listed above, it is imperative to find an oxygen storage material that best functions in the distinct

operating parameters utilized. Therefore, it is highly advantageous to specifically tailor oxygen carriers to the desired application, including temperature and atmospheric control.

Perovskite-like oxides of the ABO_3 form are among the most commonly studied oxygen storage materials given their robust stability through the uptake/release process. The presence of oxygen vacancies in a typical perovskite carrier allows for easy oxygen transport and its reduction only requires a slight rearrangement of atoms. As such, perovskites are efficient oxygen carriers due to rapid oxygen uptake/release at reasonably low operating temperatures while other oxygen carriers require higher temperatures and more elaborate structural changes.^{10–20}

Most perovskite oxygen carriers have similarities in their composition. The A-site is often occupied by a rare-earth or alkaline-earth element in a dodecahedral coordination, whereas the B site is usually a redox-active transition metal (i.e. Mn,^{10–13} Fe,^{16,17} and Co (ref. 18–20)). A-site and B-site substitution are both routine and can be performed on a stoichiometric level, such as in double perovskites,^{10–12} or on the dopant level.^{13,16} The possibility of doping at the A and B-sites, with a variety of elements, enables the calibration of key properties and creates an endless amount of potential oxygen carriers that would require both synthesis and characterization. Developing an understanding of these doping effects in relevant systems are an effective strategy to mitigate synthetic hurdles.

State-of-the-art perovskitic oxygen carriers found in the literature can achieve oxygen storage capacities between 2–4 wt%: a brief selection is listed in Table 1. Chemical substitution and doping in these base materials can be successful in increasing the rate of O_2 release or the oxygen storage capacity. To achieve these high oxygen storage capacities, the materials oftentimes rely on high concentrations of O_2 in their oxidation stream or a nonzero amount of H_2 in their reduction stream. While allowing for the most oxygen uptake and release possible in the system, the use of pure O_2 as an oxidant and/or 5% H_2 as a reductant is not feasible for all processes. For instance, materials used in ASU's for combustion processes will typically be exposed to air as a cost-effective source for O_2 uptake and an inert gas that will not partake in combustion for O_2 release.⁹

As shown in Table 1, the $Sr_{1-x}Ca_xFeO_{3-\delta}$ system is best equipped for our realistic air separation conditions.¹⁶ As the lone work on this system, Miura et al., report the oxygen storage capacities at 550 °C of four distinct $Sr_{1-x}Ca_xFeO_{3-\delta}$ samples ($x = 0, 0.20, 0.24, 0.40$), using air/ N_2 and air/5% O_2 as oxidant/reductant streams in a pressure-swing adsorption process. They found that the calcium inclusion into $SrFeO_{3-\delta}$ allows for an increase in the oxygen storage capacity of their materials at 550 °C and that a specific system ($x = 0.24$) undergoes changes in total storage capacity and release kinetics. However, additional temperatures and calcium values are not fully studied. The high oxygen storage capacity, rapid rate of reduction, and relative abundance/cost of the component elements made this material system attractive to comprehensively study the unique role Ca plays in the oxygen storage.

In this work, we begin our study with a focus on the role of Ca content on the physical structure and predictions of oxygen vacancy energies of the perovskite materials by utilizing density functional theory as a computational tool. By doing so, we establish a correlation between the oxygen vacancy formation energy descriptor and the material's actual oxygen release property

through study at multiple temperatures. In addition, we demonstrate the cyclability of this system and provide insights towards the origin of its oxygen storage capabilities. Using our findings, we achieve oxygen storage capacities of 1.51–2.41 wt%, the highest currently found in the literature at moderate cycling conditions (400–700 °C, air/N₂).

Experimental

Synthesis of Sr_{1-x}Ca_xFeO_{3-δ} oxygen carriers

To synthesize the Sr_{1-x}Ca_xFeO_{3-δ}, a modified traditional high-temperature solid state reaction was utilized.¹⁷ For a given sample, stoichiometric amounts of strontium(II) carbonate [SrCO₃, 99.9%, Sigma-Aldrich], calcium(II) carbonate [CaCO₃, 99.5%, Alfa-Aesar] and iron(III) oxide [Fe₂O₃, 99.9%, Alfa-Aesar] were added to an agate mortar and were ground until the mixture was homogeneous (approx. 10–15 min). Once homogenized, the mixture was added to a 13 mm pellet die assembly and was pressed in a manual Carver, Inc. Pellet Press (#4350.L) at a pressure between 3–4 metric tons for 15 min. Pellets were removed from the die assembly and heated at 850 °C at a rate of 1.5 °C min⁻¹ and held for 40 h in an alumina crucible under ambient air pressure. Following pre-treatment, the pellets were ground, pelletized, and heated to 1100 °C. The samples were held at temperature for 64 h. Upon completion, the crucible was cooled in air to room temperature, was removed from the furnace, the pellet ground using a mortar and pestle into a black powder, and stored in a vial for later use.

Material characterization

Synchrotron-based powder X-ray diffraction was measured on Beamline 17-BM at Advanced Photon Source (APS), Argonne National Laboratory. The X-ray wavelength was 0.24136 Å. Operating in a transmission geometry, the beamline is equipped with a PerkinElmer amorphous silica area detector at a diffraction distance of 0.7 m. Gathered image data was integrated using GSAS-II to a 2-theta vs. intensity format.²¹ In addition, GSAS-II was used to perform whole pattern Rietveld analysis to determine the unit cell parameters and the relative phase composition of the samples.

X-ray photoemission spectroscopy (XPS) experiments were conducted on a PHI 5600ci spectrometer equipped with a hemispherical electron analyzer and Al Kα (1486.6 eV) radiation source. The powder samples were prepared on double-sided carbon tape for XPS analysis. All binding energies were calibrated to the C 1s at 284.6 eV. The XPS fitting analysis was carried out using XPSPEAK software.

Oxygen temperature programmed desorption experiments were performed using a Micromeritics 2950 system connected to a Pfeiffer Vacuum Thermostat Mass Spectrometer. To begin, a quartz sample tube was packed with quartz wool and a known amount of the sample (approx. 200 mg). The sample was then heated to 800 °C at a rate of 10 °C min⁻¹ under air flow. The sample remained at 800 °C for 1 hour and then subsequently cooled rapidly under air flow. Once room temperature was reached, the gas flow was switched to He and the system was allowed to equilibrate for 30 min. The system was then heated to 1050 °C with a 10 °C min⁻¹ heating rate

and the outlet gas was analyzed by the mass spectrometer. Following the ramp, the system was cooled rapidly down to ambient temperature.

A Mettler Toledo DSC/TGA 3+ was used for thermogravimetric analysis (TGA). Prior to any cycling experiments, approximately 50 mg of sample was added to a platinum pan and was twice heated at a rate of $10\text{ }^{\circ}\text{C min}^{-1}$ to $800\text{ }^{\circ}\text{C}$ under flowing air followed by a switch to a nitrogen flow to reduce the samples. For subsequent cycling experiments, the pan was heated at a rate of $20\text{ }^{\circ}\text{C min}^{-1}$ under flowing air to 100 degrees below the desired temperature. Once within 100 degrees, the rate was lowered to $10\text{ }^{\circ}\text{C min}^{-1}$ to reach the desired temperature. The atmosphere was cycled between air and nitrogen at 75 sccm while the heat flow and weight loss were monitored.

Energy dispersive X-ray spectroscopy (EDX) was collected on a FEI Quanta 600 FEG scanning electron microscope to provide elemental analysis of the as-made samples. These ratios agree with the ratios of the starting oxide and carbonate precursors. We have chosen to report our samples' chemical formulas throughout the manuscript using the ratios of our starting reagents for readability.

Computational methods

First-principles spin-polarized density functional theory (DFT) total energy calculations were carried out as implemented in the Vienna Ab Initio Simulation Package (VASP) code.²² This implementation includes total energy and atomic force calculations. The core electrons of each atom were treated as a frozen atomic core via the projector-augmented wave (PAW) method.²³ For Sr, Ca, Fe and O, we used PAW potentials acting on 10 ($4s^2$, $4p^6$ and $5s^2$), 10 ($3s^2$, $3p^6$ and $4s^2$), 8 ($4s^2$ and $3d^6$) and 6 ($2s^2$ and $2p^4$) outer core electrons. The Kohn–Sham one electron valence eigenstates were expanded in terms of plane-wave basis sets with a cutoff energy of 500 eV using Monkhorst–Pack k-point scheme.²⁴ We used the hybrid functional HSE06 to calculate the exchange–correlation energy which shows predictive power in describing exchange interactions in transition metal oxides including perovskites.^{25,26} It was introduced by Heyd, Scuseria and Ernzerhof that one quarter of the Perdew–Burke–Ernzerhof (PBE) short-range exchange is replaced by exact exchange while the full PBE correlation energy is included. The range separation parameter is set to $\mu = 0.2\text{ \AA}^{-1}$.

For reference, the 5-atom cubic $1 \times 1 \times 1$ unit cell of SrFeO_3 material with Pm3m space group symmetry (Fig. 1) was optimized to determine basic properties. Both the ion positions and cell volume were relaxed until the total force on each atom was $<0.03\text{ eV \AA}^{-1}$. The predicted lattice parameters of $a = b = c = 3.851\text{ \AA}$ is in excellent agreement with the experimental value of $3.851\text{--}3.870\text{ \AA}$.^{27–29} The calculated magnetic moment of Fe is $3.71\text{ } \mu_{\text{B}}$ which compares well with the experimental value of $3.1 \pm 0.1\text{ } \mu_{\text{B}}$ (ref. 30) and a calculated value of $3.70\text{ } \mu_{\text{B}}$ using the LSDA+U method.³¹ The overestimation of the computed magnetic moment may be attributed to the presence of a helical magnetic ordering of the Fe^{4+} sublattice which makes it difficult to accurately predict the magnetic moment of the iron atoms. This incommensurate helical structure of SrFeO_3 is a result of a delicate competition between long-range ferromagnetic and short-range antiferromagnetic interactions.³²

The PDOS yields a half-metallic character for SrFeO₃ with gap in the minority spin channel. The majority spin channel contains bands spanning the Fermi level formed mostly by hybridization of Fe 3d and O 2p states. In the minority channel, the top of the valence band is dominated by O 2p states whereas the reverse is true for the bottom of the conduction band.

To simulate the A-site substituted materials, the simple cubic unit cell was extended to $2 \times 2 \times 2$ supercell. The 40-atom cubic supercell enabled a substitution level of 12.5, 25, 37.5 and 50%. These concentrations bracket the measured values allowing efficient comparison with experiments. The reciprocal space integration was performed by a sampling of the Brillouin zone with $4 \times 4 \times 4$ k-point grid. For a given concentration, we enumerated all of the possible A-site substitution of Ca within the 40 atom supercell. The DFT-HSE06 model was employed to calculate the energy cost of removing oxygen for each optimal doped structure. The oxygen vacancy formation energy in the lattice which was used as a metric for the ease of oxygen removal is defined as:

The last and first terms represent the energy of the perfect crystal structure and its defective counterpart with one oxygen vacancy created, respectively, while E_{O_2} is the lowest energy triple state of the oxygen molecule. Following previous efforts,^{33,34} energetic adjustment was carried out in order to address the problem of DFT calculations of O₂. The corrected value of -8.50 eV derived from the PBE functional using the PAW pseudopotential was instead used for the total energy of O₂. Bader charge and density of states analyses were performed to analyze the electronic distribution.³⁵ In our calculations, we considered all unique vacancy sites for each doped structure and averaged the calculated $\Delta E_{f,vac}$.

In the case where multiple phases were present in the experimental samples, only the more dominant case (i.e. perovskite phase) was considered. The brownmillerite structure is oxygen deficient and acts as the reduced phase for the oxygen removal process being studied, and therefore should not greatly contribute to our oxygen vacancy formation energy calculations. By only including the perovskite phase, we can investigate the effect of the Sr/Ca ratio on this and the other properties we studied directly.

It should be noted that explicit use of the orthorhombic ABO₃ phase will not significantly affect our results. To quantitatively support this assertion, we calculated the oxygen vacancy formation energy of a supercell with an orthorhombic structure (Pnma) containing same number of atoms as the cubic cell for $x = 0.5$, Ca doping. We employed the PBE+U to relax the structures followed by single point HSE06 total energy calculations. The resulting average vacancy formation energy (3.86 ± 0.04 eV) is comparable to the cubic cell (3.68 ± 0.12 eV) calculated at the same level of theory. The cubic and orthorhombic phases are not significantly different from a structural standpoint; therefore, considering only the more dominant phase is sufficient to capture the physics of oxygen vacancies and electronic properties in Sr_{1-x}Ca_xFeO₃.

Results and discussion

Predicted oxygen vacancy formation energies

Given literature interest in the $\text{Sr}_{1-x}\text{Ca}_x\text{FeO}_3$ system as oxygen carriers,¹⁶ we addressed the role of Ca substitution in the SrFeO_3 lattice from a computational standpoint, first considering all unique arrangements of the atoms within the A site of the lattice. As shown in Fig. 1, for substitution fractions ranging from $x = 0.125$ to $x = 0.5$, we found the lattice arrangements that have the lowest energy. The motifs with the lowest energy tend to have all the dopants localized within a specific Sr sublattice in the supercell. Structures with more isotropic distribution (e.g. alternating Sr and Ca on the A sites for $x = 50\%$) were found to be slightly unfavorable from an energetic standpoint by 20 to 127 meV depending on Ca concentration (see Fig. S1). Following previous efforts,^{36–39} we use the oxygen vacancy formation energy, $\Delta E_{f,\text{vac}}$, as a key metric to evaluate the propensity towards oxygen release. It should be noted that enhancing oxygen diffusion within the bulk is a mandatory capability to improve the material performance considering diffusion from the bulk to the surface is a key step to oxygen release. Oxygen requires lattice vacancies to diffuse since its large size precludes it to move through the interstices.

Fig. 2 displays calculated $\Delta E_{f,\text{vac}}$ versus Ca content (x) in SrFeO_3 along with the degree of delocalization of charges. The predicted $\Delta E_{f,\text{vac}}$ generally decreases indicating that the oxygen escapes more easily with increasing Ca content. We provide theoretical confirmation that the ability of perovskite material considered here to allow for bulk oxygen diffusion and its efficient surface release could be associated with the energetic penalty to form oxygen vacancies.

To obtain a semi-quantitative understanding of the general trends in electronic distribution, the effective Bader charges were calculated and averaged over all ions of the same type. For all the perfect perovskites, the effective charges of Sr/Ca (1.64–1.65e) and Fe (1.67–1.73e) are smaller than their formal charges of +2e and +3e, respectively. On O, the effective charge is reduced (–1.10 to –1.13e) with respect to the formal charge of –2e. These results indicate a degree of covalent contribution to both Sr/Ca–O and Fe–O chemical bonding with the latter covalency predicted to be more pronounced. An interesting behavior was observed from the analysis of electronic density rearrangement after an oxygen vacancy is formed. Both Sr and Ca ions undergo very minor changes in response to oxygen vacancy. On the average, the variation is not more than $\sim 0.01e$. The Fe ions are noticeably oxidized with the effective charges increasing by up to 0.06e. The O sublattice, on the other hand, is more involved in the delocalization of the charge with each oxygen ion accommodating 0.04–0.06e upon vacancy formation. Following Muñoz-García et al.,⁴⁰ the degree of delocalization γ was evaluated at all dopant concentrations: $\gamma = (N - 1)(q_{\text{ave,perfect}} - q_{\text{ave,defective}})/q_{\text{ave,perfect}}$, where N is the number of oxygen in the perfect cell, while $q_{\text{ave,perfect}}$ and $q_{\text{ave,defective}}$ refer to the average Bader charge of the oxygen in the perfect and defective cell, respectively. This quantity represents the extent to which the O sublattice absorbs the excess charge. We found a general reduction in γ with decreasing vacancy formation energy (Fig. 2). This implies that the addition of Ca leads to lesser delocalization of electrons upon formation of vacancy. While the trend in our predicted vacancy formation energy closely relates to the ease in oxygen removal, the one for charge delocalization is rather counterintuitive. Previous efforts showed that increasing γ typically accompanies the lowering of $\Delta E_{f,\text{vac}}$.^{36–39} The fact that this leads to the opposite effect may be due to the inability of the oxygen ions to absorb a level of electron density beyond what is required under ideal circumstances.⁴¹ A subtle effect of doping is the general, albeit slight, increase in the ionicity of Fe–O with increasing Ca concentration. For the perfect lattice, Fe and O have Bader charges of +1.67e and –1.10e for $x = 0$ reaching the level of +1.73e and –1.13e at $x = 0.5$. As the Fe–O bond becomes slightly more

ionic, it is not possible to add more negative charge to the O sublattice since it is already saturated with electrons.⁴²

To further allow for the investigation of the electronic structure changes associated with increasing Ca content, the partial density of states (PDOS) for the perfect perovskites were calculated. The PDOS for the parent material in Fig. 3 show overlapping states between the Fe 3d and O 2p in the valence region. The upper region is dominated by O 2p with some Fe 3d contribution. At lower energies, the O 2p states diminish whereas contribution from Fe and Sr become more dominant. The valence band character paints an ionic–covalent picture of the parent material which is consistent with the Bader charge analysis. In addition, the pristine SrFeO₃ exhibits semi-metallic behavior as shown by the band opening on the minority spin states with predicted band gap of 1.69 eV (Fig. 3f). Introduction of Ca results into two distinct changes in the PDOS; the reduction of Sr 5s and 4p peaks around –35 and –16 eV and the appearance of new s and p peaks at –42 and –22 eV (Fig. 3a–e). Both changes originate from the replacement of Sr by Ca atoms. While the additional low-lying energy split of the s and p states are observed, the HSE06 calculations show that the various Ca-substituted counterparts retain their semi-metallic behavior (Fig. 3g–j). This means that the presence of Ca will negligibly impact the electronic conductivity of the material. The band gaps of the minority spin states are not significantly different, namely, 1.68, 1.67, 1.66, and 1.65 eV for 12.5%, 25%, 37.5% and 50% Ca, respectively. Thus, the reduction in $\Delta E_{f,vac}$ upon Ca incorporation is complemented by the retention of the electronic conductivity.

Materials synthesis and physical characterization

Using our computational findings, materials with higher Ca contents were most attractive for further study as oxygen carriers. To corroborate our theoretical study, Sr_{1-x}Ca_xFeO_{3- δ} materials were experimentally prepared with various Ca contents of $x = 0-0.4$ by a solid-state reaction. Unlike sol–gel and autocombustion methods,² this traditional method produces large particles (5 μ m). It has been known that the rate and capacity of oxygen uptake/release are affected by the particle size for similar systems.⁴³ By keeping the particle size large, our materials suffer from slower kinetics as the oxygen must traverse through the structure, but we mitigate any kinetic differences between our samples due to particle size. In addition, the decreased surface area allows us to reduce the amount of adsorbed species on the Sr_{1-x}Ca_xFeO_{3- δ} materials. This can bring a greater focus on how oxygen release and uptake is related to the Ca-doping level, which should have the greatest effect on lattice oxygen.

Herein we employed a synthesis method requiring a pre-treatment at 850 °C prior to the final synthesis temperature of 1100 °C. This pre-treatment step, used in our works,¹⁷ assists in producing better homogeneity in our samples through the inclusion of intermittent grinding following the decomposition of the carbonate salts and release of any adsorbed water. This allows for a pellet that has less barrier to solid-state diffusion when the temperature was raised to 1100 °C, leading to a more uniform sample. To verify our assumption that the Sr/Ca/Fe ratio remains constant through the synthesis, EDX was used to support the use of the initial precursor ratios to succinctly define each material studied in this manuscript (Fig. S2).

Synchrotron powder X-ray diffraction was used to identify the bulk crystal structure of our as-synthesized $\text{Sr}_{1-x}\text{Ca}_x\text{FeO}_{3-\delta}$ materials (stopping at $x = 0.40$). As represented in Fig. 4, all materials are primarily perovskitic. While true perovskites are cubic, our material resembles a common permutation as an orthorhombic structure according to Rietveld analysis, although the crystallographic differences between the structures are minimal, as shown in Fig. S3. In addition, the A-site substitution of Ca^{2+} for Sr^{2+} yields a linear decrease in the unit cell size, obeying Vegard's law. This can be observed by 2-theta shifts in the pXRD pattern and comparisons in Fig. S4.† Higher Ca doping levels ($x > 0.30$) also lead to the co-presence of an orthorhombic brownmillerite $\text{Ca}_{2-x}\text{Sr}_x\text{Fe}_2\text{O}_5$ species. While only a 5% impurity is observed in the $x = 0.30$ sample, roughly 40% of the $x = 0.35$ and 0.40 samples are this phase according to Rietveld refinement. Despite different synthesis methods, our observation agrees with literature findings on this system, where the emergence of this secondary phase begins at $x \geq 0.30$.¹⁶

To observe changes in surface structures, XPS measurements were conducted as a surface probe on a subset of $\text{Sr}_{1-x}\text{Ca}_x\text{FeO}_{3-\delta}$ systems ($x = 0.20, 0.25, 0.30$). As shown in Fig. S5, the O 1s XPS for all samples exhibit broad peaks ranging from 526 to 536 eV. Four distinguished components were applied to deconvolute the broad spectra, which are lattice O^{2-} at 528.5 eV, surface adsorbed oxygen species $\text{O}_2^{2-}/\text{O}^-$ around 530.5 eV, weakly bound hydroxyl OH^- or carbonate CO_3^{2-} species at 531.8 eV and adsorbed molecular water at 533.1 eV.⁴⁴⁻⁴⁶ Both the lattice oxygen and adsorbed $\text{O}_2^{2-}/\text{O}^-$ species with lower binding energy exhibit a 10% decrease as the calcium dopant of the samples increases. A significant increase in adsorbed OH^- and CO_3^{2-} species from 21.5% to 40.8% was observed. Therefore, the O 1s XPS analysis suggests there is a higher ratio of oxygen vacancies in perovskite samples with higher Ca contents, as expected. This suggests the oxygen vacancy formation energy will be lower, originating from a higher distortion of lattice structure induced by Ca dopants, which is also consistent with the computational findings.

Additionally, the Sr 3d core level spectra were fitted with three Sr components for two doublets Sr 3d_{5/2} and Sr 3d_{3/2} (Fig. S6). The peak shoulder around 131.5 eV (Sr 3d_{5/2}) is assigned to lattice Sr^{2+} , and surface SrO is responsible for the 132.8 eV feature. The high BE at 134.0 eV is correlated to the formation of surface SrCO_3 due to carbon contamination.⁴⁷⁻⁴⁹ As the Ca content increases in the perovskites, the surface adsorbed SrCO_3 builds up from 15.3% to 32.7% while the amount of lattice Sr^{2+} exhibits a 16% decrease. This is consistent with the O 1s spectra, also indicating a growth of oxygen vacancy density as Ca content increases.

Oxygen storage capacities of $\text{Sr}_{1-x}\text{Ca}_x\text{FeO}_{3-\delta}$ ($x = 0-0.4$)

To corroborate with the computational and XPS findings, we experimentally studied the oxygen storage properties of these materials by first performing oxygen temperature-programmed desorption (O_2 -TPD) to determine the overall amount of oxygen that can be released for each sample (Fig. 5). As displayed in Fig. S7, the overall O_2 storage capacity of the materials generally decreases as the calcium content increases. This suggests that δ in $\text{Sr}_{1-x}\text{Ca}_x\text{FeO}_{3-\delta}$ in the as-synthesized samples must decrease also and agrees with the findings by Miura et al.¹⁶

As shown in Fig. 5, the temperature of the overall desorption maximum gradually decreases from 627 °C to 389 °C with increasing Ca level from 0.05 to 0.40. It should be pointed out here that the shape of the TPD profile gradually changes upon calcium content increase. For perovskite

systems, there are two distinct features that classically represent α and β oxygen desorption.⁴⁷ α oxygen represents oxygen adsorbed onto the surface or grain boundaries of the oxygen carrier, requiring relatively low temperatures to remove. On the other hand, β oxygen refers to oxygen found in the lattice of the oxygen carrier. This oxygen requires higher temperatures to be removed, due to lattice disruption and oxygen transport through the material. As calcium is added to SrFeO₃, the α feature moves to higher desorption temperatures and becomes less defined. Conversely, the β feature moves to lower temperatures and becomes well-defined, explaining the overall decrease in desorption maximum as the α and β features converge. These trends are consistent with the computational measurements showing that Ca-doped SrFeO₃ materials exhibit improved O₂ release, namely, the oxygen vacancy formation energy decreases with increasing concentration of Ca.

Because the desorption maximum was altered by adjusting the Sr/Ca ratio, we determined the extent of oxygen loss due to the inert atmosphere and temperature versus the effect of temperature alone. Fig. 6 shows the TGA plots of Sr_{1-x}Ca_xFeO_{3- δ} samples as the temperature was increased to 800 °C under an air flow, followed by a switch to N₂ flow (at a rate of 10° min⁻¹). As observed in Fig. 6a, the oxygen content systematically decreases at roughly the same rate for the samples with $x < 0.30$. This experiment also confirms that samples with 15–30% Ca A-site content have the largest oxygen storage capacities upon heating to 800 °C, whereas 0–10% Ca are moderate. The as-synthesized 35% and 40% Ca materials are partially reduced, so their lower overall storage capacity is unsurprising. Additionally, samples with above 40% Ca were not fully characterized as the oxygen storage capacity greatly decreases above this threshold.

Given that these experiments start with the as-synthesized samples, it is noteworthy that some of the samples see their mass remain relatively constant between 350–400 °C. To further probe this and determine an adsorption maximum, the reduced samples were re-oxidized in the TGA under air flow (Fig. 6b). Unlike the desorption maximum in the O₂-TPD, the temperature of absorption maximum increases as the Ca content increases (from 294–460 °C for $x = 0$ –0.40). This emphasizes that the addition of Ca to the lattice destabilizes the oxidized form of the material. By analyzing the difference in the position of the TGA curve at the temperature versus the weight following reduction at 800 °C, we can estimate the maximum possible oxygen storage capacities of each sample at a given temperature by analyzing the difference in the position of the curve at the temperature versus the weight following reduction at 800 °C. For every sample, the maximum oxygen storage capacity decreases as the temperature is increased past 460 °C.

Oxygen absorption/desorption kinetics

While the above method is useful to estimate the maximum possible oxygen storage capacity, it does not take kinetics into account. Therefore, we analyzed the mass change of each sample at a specific selection of temperatures (400 °C, 450 °C, 500 °C, 550 °C, 600 °C, 700 °C) while switching between N₂ and air flow. At 400 °C, hourlong reduction and oxidation dwells were used to combat the slow kinetics expected at lower temperatures (Fig. 7a). Oxidation (<5 min) is generally more rapid than reduction, comparable amongst all experiments in the text, and will not be discussed henceforth. Specific values of oxygen release amounts and rates as functions of temperature and Ca content are listed in Tables S1 and S2. The oxygen storage capacities of the systems dropped from 2.41 wt% to 1.72 wt% as increasing Ca content from $x = 0.25$ to $x = 0.40$.

It is also important to look at shorter timeframes to determine the rate of oxygen release. The $x = 0.35$ sample has almost full release of oxygen in 20 minutes, whereas the 25% sample requires the full hour to release the 2.41 wt% O_2 and only approx. 90% done after 36 minutes.

Similarly, we explored the oxygen storage capacity at other temperatures (Fig. 7b–f). At 450 °C, samples ranging from $x = 0.20$ to $x = 0.35$ samples are the most attractive. Similar to our findings at 400 °C, the highest storage capacities over 30 minutes are achieved by the more Sr-rich samples in this range ($x = 0.20$, 2.37 wt%), while kinetically the more Ca-rich systems are preferred ($x = 0.35$, 1.90 wt%). Given this dichotomy, the 30% or 25% Ca samples are overall the most effective oxygen carriers at this temperature.

This thought process could be applied to the other temperatures in our study as well. At 500 °C, sample ranges from $x = 0.15$ to $x = 0.30$ are most interesting, with $x = 0.15$ providing 2.26 wt% O_2 over 30 minutes and $x = 0.30$ being most rapid (1.77 wt% in <2 minutes). At 550 °C, sample ranges from $x = 0.10$ to $x = 0.25$ are most interesting, with $x = 0.10$ and $x = 0.15$ both providing 2.04 wt% O_2 over 20 minutes and $x = 0.25$ being most rapid (1.84 wt% in <2 minutes). At 600 °C, sample ranges from $x = 0.10$ to $x = 0.20$ are again the most interesting, with $x = 0.10$ providing 1.90 wt% O_2 over 20 minutes and $x = 0.20$ being most rapid (1.78 wt% in <2 minutes). Finally, for 700 °C, sample ranges from $x = 0.05$ to $x = 0.15$ are again the most interesting, with $x = 0.05$ providing 1.55 wt% O_2 over 15 minutes and $x = 0.20$ being most rapid (1.36 wt% in <2 minutes). In all cases, we would suggest the systems with intermediate calcium contents to take advantage of both fast kinetics and still relatively high oxygen storage capacities.

While studying these oxygen storage systems, we determined two factors that should be explicitly mentioned which can aid in material choice for a given application. First, the kinetics are faster overall as the temperature setpoint is increased, meaning the difference between release time between the “slowest” and “fastest” samples is less exaggerated. Second, the maximum oxygen storage capacity for a given system decreases as the temperature is increased. This was also observed in our ramped reoxidation experiments in the TGA. In addition, the rapid drop in oxygen content found in the $x = 0.25$ through $x = 0.40$ samples in those TGA measurements were predictive of similar behavior in oxygen storage capacities in cycling as well.

Structural cyclability through in situ synchrotron pXRD

For each of these samples, the oxygen storage capacity remains consistent through multiple cycles (Fig. S8), however it was unclear if the perovskite structure is retained through a single cycle. We used in situ synchrotron X-ray Diffraction (HT-XRD) experiments on $SrFeO_3$, $Sr_{0.8}Ca_{0.2}FeO_3$, and $Sr_{0.7}Ca_{0.3}FeO_3$ under gas switch from air to He atmosphere to probe this question (Fig. 8). By switching the gas flow over our sample from simulated air to He, we were able to simulate our TGA experiments at 400 °C, 550 °C, and 800 °C. These temperatures were chosen to simulate range of temperatures representing the broad usefulness of these materials, with a selection of compositions that would provide rapid oxygen storage and release at each temperature. It was determined that the reduction occurring at increased temperature leads to the formation of a brownmillerite-type $Ca_{2-x}Sr_xFe_2O_5$ phase. It is notable that the reversible transition between brownmillerite-like $Ca_{2-x}Sr_xFe_2O_5$ and perovskite $Sr_{1-x}Ca_xFeO_3$ is not present during all 9 experiments (Fig. 8 and S9, S10).

At 800 °C, oxidation was rapid for the $x = 0$ and $x = 0.20$ samples, occurring in less than one minute, however, reduction was faster for the $x = 0.20$ sample than SrFeO_3 (<1 min compared to 3+ min for full reduction). For the $x = 0.30$ sample, the sample is relatively unchanged during gas switch, as less than 0.14 wt% O_2 is cyclable at this temperature. Even under the simulated air flow, the sample did not revert to the perovskite structure.

However, the 550 °C and 400 °C cycling experiments may better suggest the role of these observed structural changes during the release and uptake of oxygen. For the parent sample, the expected amount of oxygen released is 1.06 wt% and 0.84 wt%, respectively. However, within the first minute after switching to inert flow, we expect a loss of 0.45 wt% at 550 °C and we see no observable structural change at this timepoint in the HT-XRD experiment or throughout the entirety of the 400 °C experiment. This suggests that labile surface oxygen species contribute to at least the first ca. 0.8 wt% of cyclable oxygen in SrFeO_3 .

For the $x = 0.20$ sample, these designations are not conclusive as structural changes are observed at all timepoints at all three temperatures. For example, at 550 °C, the perovskitic structure was no longer observable by XRD after 1 minute under He flow. From our TGA findings, 45% of the cyclable oxygen in $\text{Sr}_{0.8}\text{Ca}_{0.2}\text{FeO}_3$ should be released during this timeframe. At 400 °C, it was only accompanied by a slight increase in brownmillerite-type oxide over 20 minutes, despite an observed release of over 1 wt% O_2 in the TGA. This correlates with the O_2 -TPD that the initial loss/uptake is α -oxygen, or surface species, with the remaining O_2 originating as lattice oxygen. This description may also explain the shoulder observed in the O_2 -TPD for the $x = 0.20$ sample and is consistent with our findings from XPS.

For the $x = 0.30$ sample, the structural transition accompanies both the oxygen release at 400 °C and 550 °C. Unlike the other the $x = 0$ and $x = 0.20$ systems, more information is elucidated by interpreting the transition during reoxidation of the samples, as it is a slower structural transition than its reduction. While only 0.50 wt% O_2 is cyclable at 550 °C, the brownmillerite-type structure persists with a slight transition to perovskite. The inability to fully reoxidize to perovskite is observed in the 400 °C experiment as well, likely because roughly 5% of the sample begins in the brownmillerite structure at room temperature (Fig. 4).

Conclusions

In conclusion, we show that temperature tunability of rapid oxygen uptake/release can be achieved in the $\text{Sr}_{1-x}\text{Ca}_x\text{FeO}_{3-\delta}$ system by altering the Ca^{2+} content of material both computationally and experimentally. We reveal the effectiveness of using oxygen vacancy creation energy as a theoretical descriptor to predict the oxygen release properties of the $\text{Sr}_{1-x}\text{Ca}_x\text{FeO}_{3-\delta}$ system, using a hybrid functional based DFT. Encompassing a temperature range of 400 °C to 700 °C, an increase in x lowers both the temperature of maximum desorption and the ideal temperature for reversible oxygen uptake/release even at oxidizing and reducing conditions that are much milder than the higher OSC perovskite oxygen carriers that can be found in the literature. We theorize that this is partially due to an increase in surface oxygen species, as determined by XPS and visualized by using in situ pXRD in conjunction with TGA. Our in situ pXRD work also establishes the rapid and robust cyclability between the perovskite and brownmillerite structures for the calcium-doped systems. Overall, the choice of

$\text{Sr}_{1-x}\text{Ca}_x\text{FeO}_{3-\delta}$ oxygen carrier depends on the specific application and desired operating temperature. The largest oxygen storage capacities will be achieved by the low Ca^{2+} samples, $x = 0.05$, but kinetically, higher values of x are desired. Functionally, we suggest the use of $x = 0.30$ or $x = 0.25$ at $450\text{ }^\circ\text{C}$ or $500\text{ }^\circ\text{C}$ as the materials release over 2 wt% of O_2 in only 4 minutes and 2 minutes, respectively.

Disclaimer

This work was funded by the Department of Energy, National Energy Technology Laboratory, an agency of the United States Government, through a support contract with the Leidos Research Support Team (LRST). Neither the United States Government nor any agency thereof, nor any of their employees, nor LRST, nor any of their employees, makes any warranty, expressed or implied, or assumes any legal liability or responsibility for the accuracy, completeness, or usefulness of any information, apparatus, product, or process disclosed, or represents that its use would not infringe privately owned rights. Reference herein to any specific commercial product, process, or service by trade name, trademark, manufacturer, or otherwise, does not necessarily constitute or imply its endorsement, recommendation, or favoring by the United States Government or any agency thereof. The views and opinions of authors expressed herein do not necessarily state or reflect those of the United States Government or any agency thereof.

Conflicts of interest

There are no conflicts to declare.

Acknowledgements

This work was performed in support of the US Department of Energy's Fossil Energy Gasification Research Program. The Research was executed through the NETL Research and Innovation Center's Advanced Reaction Systems field work proposal. Research performed by Leidos Research Support Team staff was conducted under the RSS contract 89243318CFE000003. The authors also thank Dr Wenqian Xu for assistance in collection of synchrotron XRD work. This research used resources of the 17-BM beamline of the Advanced Photon Source, a U.S. Department of Energy (DOE) Office of Science User Facility operated for the DOE Office of Science by Argonne National Laboratory under contract no. GUP-56805.

References

1. X. Zhu, K. Li, L. Neal and F. Li, ACS Catal., 2018, 8, 8213–8236.
2. S. Royer, D. Duprez, F. Can, X. Courtois, C. Batiot-Dupeyrat, S. Laassiri and H. Alamdari, Chem. Rev., 2014, 114, 10292–10368.
3. S. Pei, M. S. Kleefisch, T. P. Kobylinski, J. Faber, C. A. Udovich, V. Zhang-McCoy, B. Dabrowski, U. Balachandran, R. L. Mieville and R. B. Poeppel, Catal. Lett., 1995, 30, 201–212.
4. A. J. Jacobson, Chem. Mater., 2010, 22, 660–674.

5. C. Sun, R. Hui and J. Roller, *J. Solid State Electrochem.*, 2010, 14, 1125–1144.
6. S. Keav, S. Matam, D. Ferri and A. Weidenkaff, *Catalysts*, 2014, 4, 226–255.
7. P. T. Moseley, *Sens. Actuators, B*, 1992, 6, 149–156.
8. N. Barsan, D. Koziej and U. Weimar, *Sens. Actuators, B*, 2007, 121, 18–35.
9. J. Tollefson, *Nature*, 2018, 557, 622–623.
10. T. Motohashi, T. Ueda, Y. Masubuchi, M. Takiguchi, T. Setoyama, K. Oshima and S. Kikkawa, *Chem. Mater.*, 2010, 22, 3192–3196.
11. A. Klimkowicz, K. Świerczek, A. Takasaki, J. Molenda and B. Dabrowski, *Mater. Res. Bull.*, 2015, 65, 116–122.
12. T. Motohashi, Y. Hirano, Y. Masubuchi, K. Oshima, T. Setoyama and S. Kikkawa, *Chem. Mater.*, 2013, 25, 372–377.
13. B. Bulfin, J. Vieten, D. E. Starr, A. Azarpira, C. Zachäus, M. Hävecker, K. Skorupska, M. Schmücker, M. Roeb and C. Sattler, *J. Mater. Chem. A*, 2017, 5, 7912–7919.
14. S. Räsänen, O. Parkkima, E.-L. Rautama, H. Yamauchi and M. Karppinen, *Solid State Ionics*, 2012, 208, 31–35.
15. K. Beppu, S. Hosokawa, K. Teramura and T. Tanaka, *J. Mater. Chem. A*, 2015, 3, 13540–13545.
16. N. Miura, H. Ikeda and A. Tsuchida, *Ind. Eng. Chem. Res.*, 2016, 55, 3091–3096.
17. J. W. Lekse, S. Natesakhawat, D. Alfonso and C. Matranga, *J. Mater. Chem. A*, 2014, 2, 2397.
18. H. Ding, Y. Xu, C. Luo, Q. Wang, S. Li, G. Cai, L. Zhang, Y. Zheng and Q. Shen, *Chem. Eng. J.*, 2017, 323, 340–346.
19. A. Klimkowicz, K. Świerczek, A. Takasaki and B. Dabrowski, *Solid State Ionics*, 2014, 257, 23–28.
20. S. Royer, H. Alamdari, D. Duprez and S. Kaliaguine, *Appl. Catal., B*, 2005, 58, 273–288.
21. B. H. Toby and R. B. von Dreele, *J. Appl. Crystallogr.*, 2013, 46, 544–549.
22. G. Kresse and J. Hafner, *J. Phys.: Condens. Matter*, 1994, 6, 8245–8257.
23. G. Kresse and D. Joubert, *Phys. Rev. B: Condens. Matter Mater. Phys.*, 1999, 59, 1758–1775.
24. H. J. Monkhorst and J. D. Pack, *Phys. Rev. B: Condens. Matter Mater. Phys.*, 1976, 13, 5188–5192.
25. J. Heyd, G. E. Scuseria and M. Ernzerhof, *J. Chem. Phys.*, 2003, 118, 8207–8215.
26. J. Hong, A. Stroppa, J. Íñiguez, S. Picozzi and D. Vanderbilt, *Phys. Rev. B*, 2012, 85, 054417.
27. J. P. Hodges, S. Short, J. D. Jorgensen, X. Xiong, B. Dabrowski, S. M. Mini and C. W. Kimball, *J. Solid State Chem.*, 2000, 151, 190–209.
28. A. E. Bocquet, A. Fujimori, T. Mizokawa, T. Saitoh, H. Namatame, S. Suga, N. Kimizuka, Y. Takeda and M. Takano, *Phys. Rev. B: Condens. Matter Mater. Phys.*, 1992, 45, 1561–1570.
29. M. J. Akhtar and R. T. A. Khan, *Mater. Charact.*, 2011, 62, 1016–1020.
30. T. Takeda, Y. Yamaguchi and H. Watanabe, *J. Phys. Soc. Jpn.*, 1972, 33, 967–969.
31. I. R. Shein, K. I. Shein, V. L. Kozhevnikov and A. L. Ivanovskii, *Phys. Solid State*, 2005, 47, 2082–2088.
32. M. Reehuis, C. Ulrich, A. Maljuk, Ch. Niedermayer, B. Ouladdiaf, A. Hoser, T. Hofmann and B. Kelmer, *Phys. Rev. B: Condens. Matter Mater. Phys.*, 2012, 85, 184109.

33. L. Wang, T. Maxisch and G. Ceder, *Phys. Rev. B: Condens. Matter Mater. Phys.*, 2006, 73, 195107.
34. Y.-L. Lee, J. Kleis, J. Rossmeisl and D. Morgan, *Phys. Rev. B: Condens. Matter Mater. Phys.*, 2009, 80, 224101.
35. G. Henkelman, A. Arnaldsson and H. Jónsson, *Comput. Mater. Sci.*, 2006, 36, 354–360.
36. A. B. Muñoz-García, M. Pavone and E. A. Carter, *Chem. Mater.*, 2011, 23, 4525–4536.
37. C. Chen, Z. M. Baiyee and F. Ciucci, *Phys. Chem. Chem. Phys.*, 2015, 17, 24011–24019.
38. Y. A. Mastrikov, M. M. Kuklja, E. A. Kotomin and J. Maier, *Energy Environ. Sci.*, 2010, 3, 1544–1550.
39. Y.-L. Lee, J. Kleis, J. Rossmeisl, Y. Shao-Horn and D. Morgan, *Energy Environ. Sci.*, 2011, 4, 3966–3970.
40. A. B. Muñoz-García, A. M. Ritzmann, M. Pavone, J. A. Keith and E. A. Carter, *Acc. Chem. Res.*, 2014, 47, 3340–3348.
41. A. M. Ritzmann, J. M. Dieterich and E. A. Carter, *Phys. Chem. Chem. Phys.*, 2016, 18, 12260–12269.
42. A. B. Muñoz-García, D. E. Bugaris, M. Pavone, J. P. Hodges, A. Huq, F. Chen, H.-C. Zur Loye and E. A. Carter, *J. Am. Chem. Soc.*, 2012, 134, 6826–6833.
43. A. Klimkowitz, K. Świerczek, T. Yamazaki and A. Takasaki, *Solid State Ionics*, 2016, 298, 66–72.
44. H. Falcon, J. A. Barbero, J. A. Alonso, M. J. Martinez-Lope and J. L. G. Fierro, *Chem. Mater.*, 2002, 14, 2325–2333.
45. N. A. Merino, B. P. Barbero, P. Eloy and L. E. Cadús, *Appl. Surf. Sci.*, 2006, 253, 1489–1493.
46. C. C. Wang, K. O'Donnell, L. Jian and S. P. Jiang, *J. Electrochem. Soc.*, 2015, 162, F507–F512.
47. P. A. W. van der Heide, *Surf. Interface Anal.*, 2002, 33, 414–425.
48. J. Kuhn and U. Ozkan, *J. Catal.*, 2008, 253, 200–211.
49. N. Yamazoe, Y. Teraoka and T. Seiyama, *Chem. Lett.*, 1981, 10, 1767–1770.

Material (family)	OSC (wt%)	Ox. Atm.	Red. Atm.	Temp. (°C)
BaYMn ₂ O _{5+δ} (ref. 10 and 11)	3.71%	O ₂ or air	5% H ₂	500
YBa(Co _{1-x} Ga _x) ₄ O _{7+δ} (ref. 14)	3.50%	O ₂	N ₂	350
Ca ₂ AlMnO _{5+δ} (ref. 12)	2.90%	O ₂	N ₂	400
Ca _{0.8} Sr _{0.2} MnO _{3-δ} (ref. 13)	~2.5%	1 bar O ₂	10 ⁻⁵ bar O ₂	800
Sr ₃ Fe ₂ O _{7-δ} (ref. 15)	~2%	5% O ₂	5% H ₂	500
Sr _{1-x} Ca _x FeO _{3-δ} (ref. 16)	~2%	Air	N ₂	550

Table 1 Contains a selection of complex metal oxide oxygen carriers reported in the literature that each represent a family of related materials.

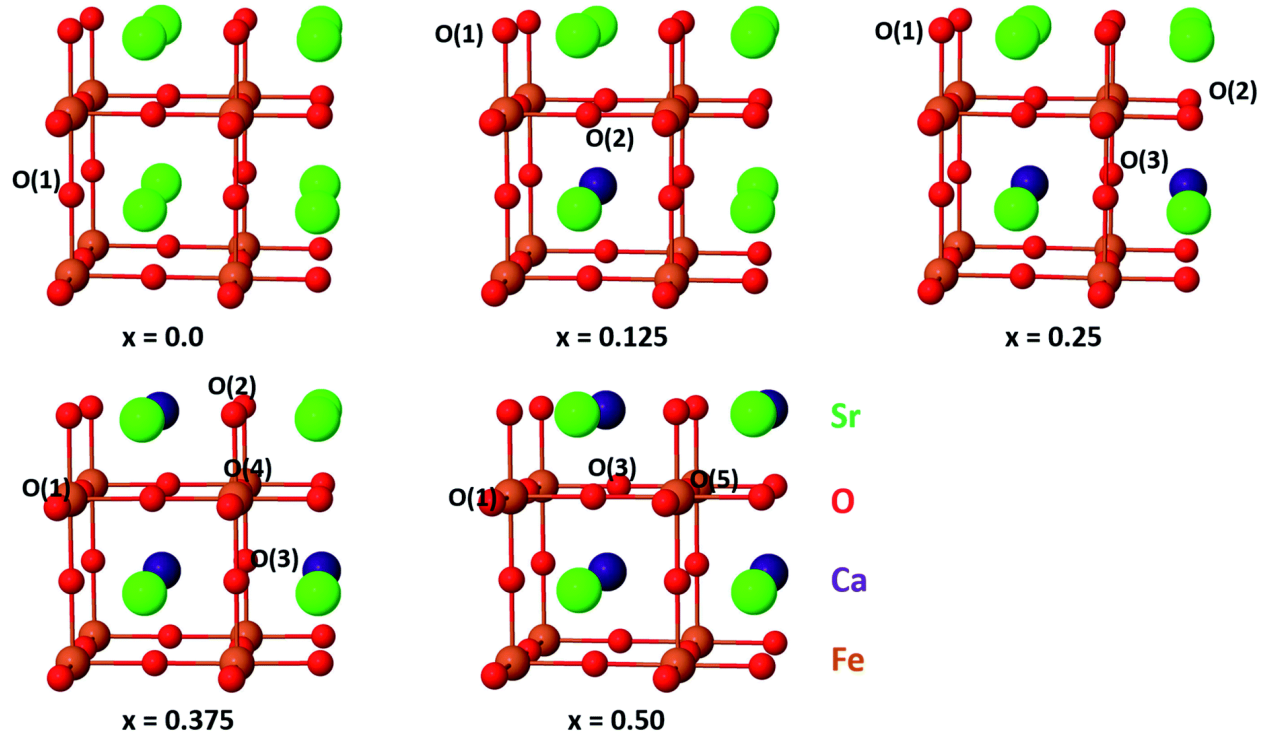


Fig. 1 Contains the lowest energy structures of the $2 \times 2 \times 2$ cubic supercells of $\text{Sr}_{1-x}\text{Ca}_x\text{FeO}_3$ obtained with HSE06. O($i = 1, 2, 3, 4, 5$) is the non-equivalent oxygen position in the materials; i is related to the number of Ca nearest-neighbor to an O (N_{Ca}), $N_{\text{Ca}} = i - 1$ and distance between O and Ca, $d(\text{O}-\text{Ca}) < 2.71 \text{ \AA}$.

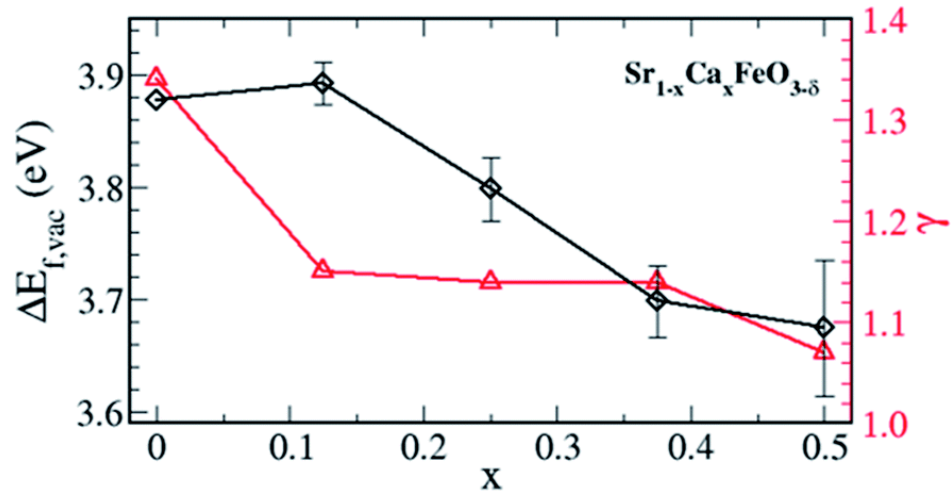


Fig. 2 Shows the degree of delocalization of charges (red, γ) plotted against oxygen vacancy formation energies (black) as a function of Ca concentration. DFT values are averaged over the low-energy cases.

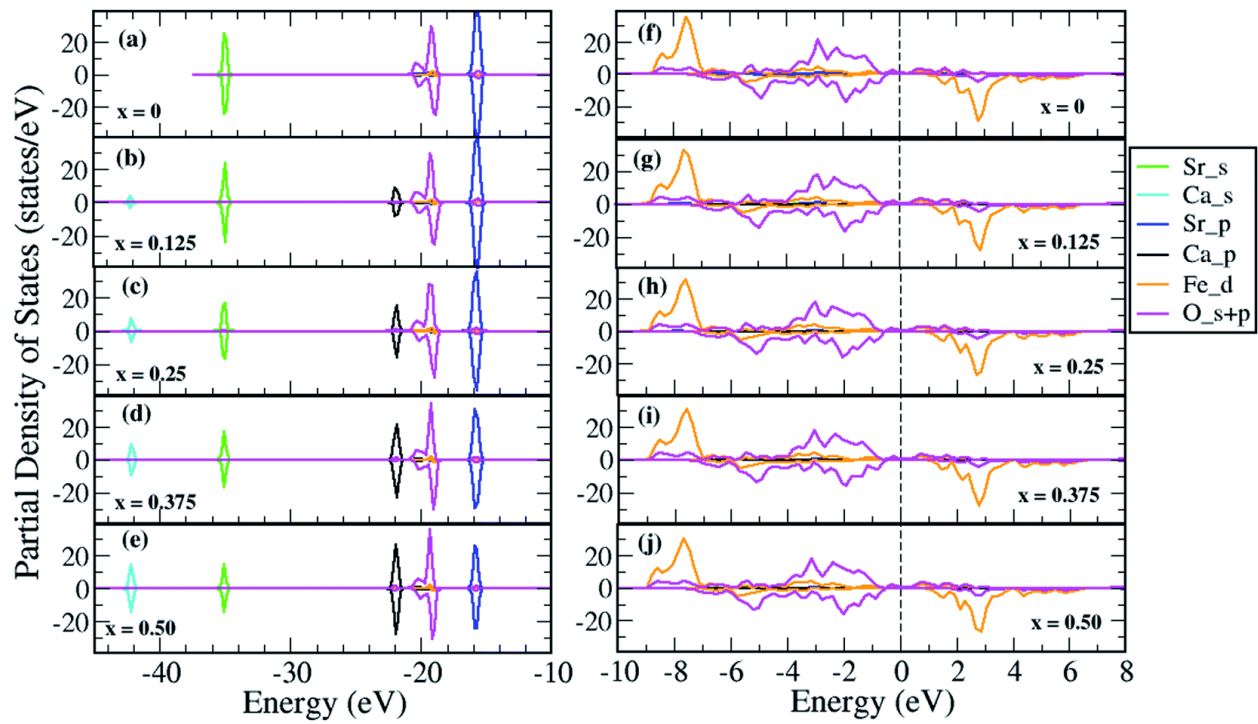


Fig. 3 Contains projected density of states for (a) $x = 0$ and the (b) $x = 0.125$, (c) $x = 0.25$, (d) $x = 0.375$, and (e) $x = 0.50$ samples. A zoomed-in region clearly showing the states relevant to bandgap calculations are shown in (f)–(j). The vertical dotted line at 0 eV indicates the Fermi level.

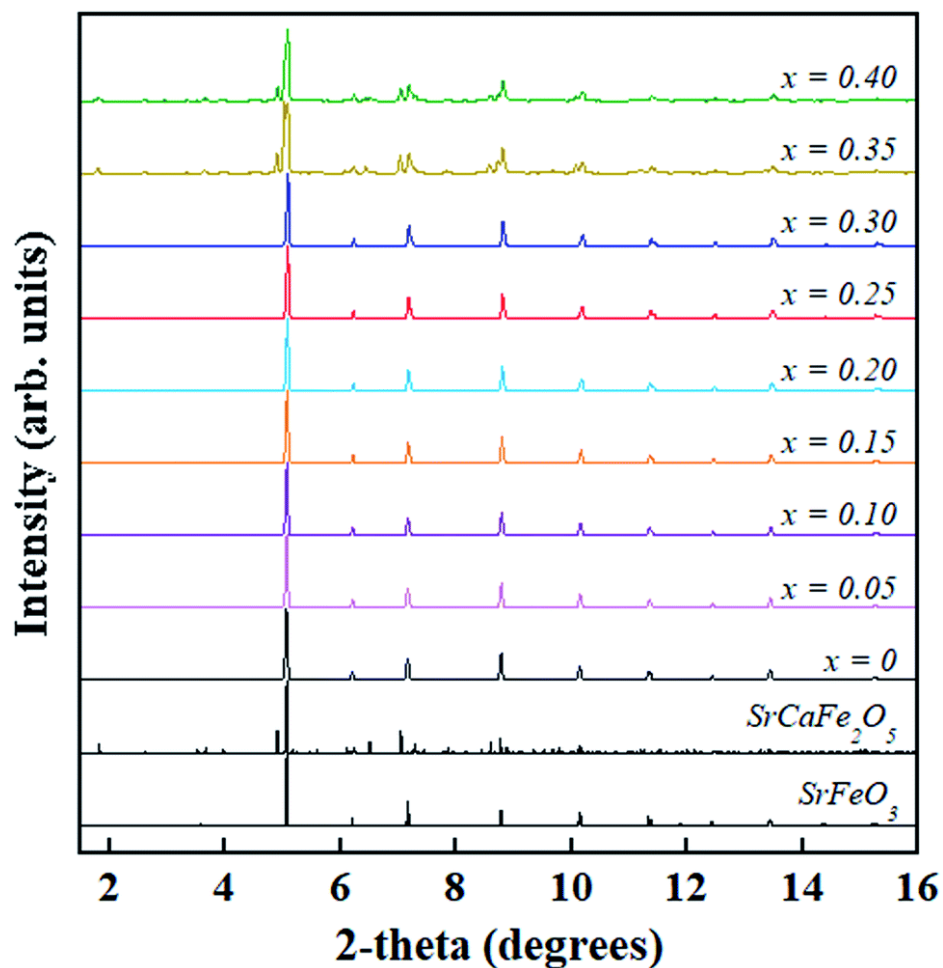


Fig. 4 Shows synchrotron powder X-ray diffraction patterns ($\lambda = 0.24136 \text{ \AA}$) for samples in the $\text{Sr}_{1-x}\text{Ca}_x\text{FeO}_{3-\delta}$ system following synthesis. Reference patterns shown correspond to orthorhombic SrFeO_3 and $\text{SrCaFe}_2\text{O}_5$. Samples with $x > 0.30$ contain both phases referenced.

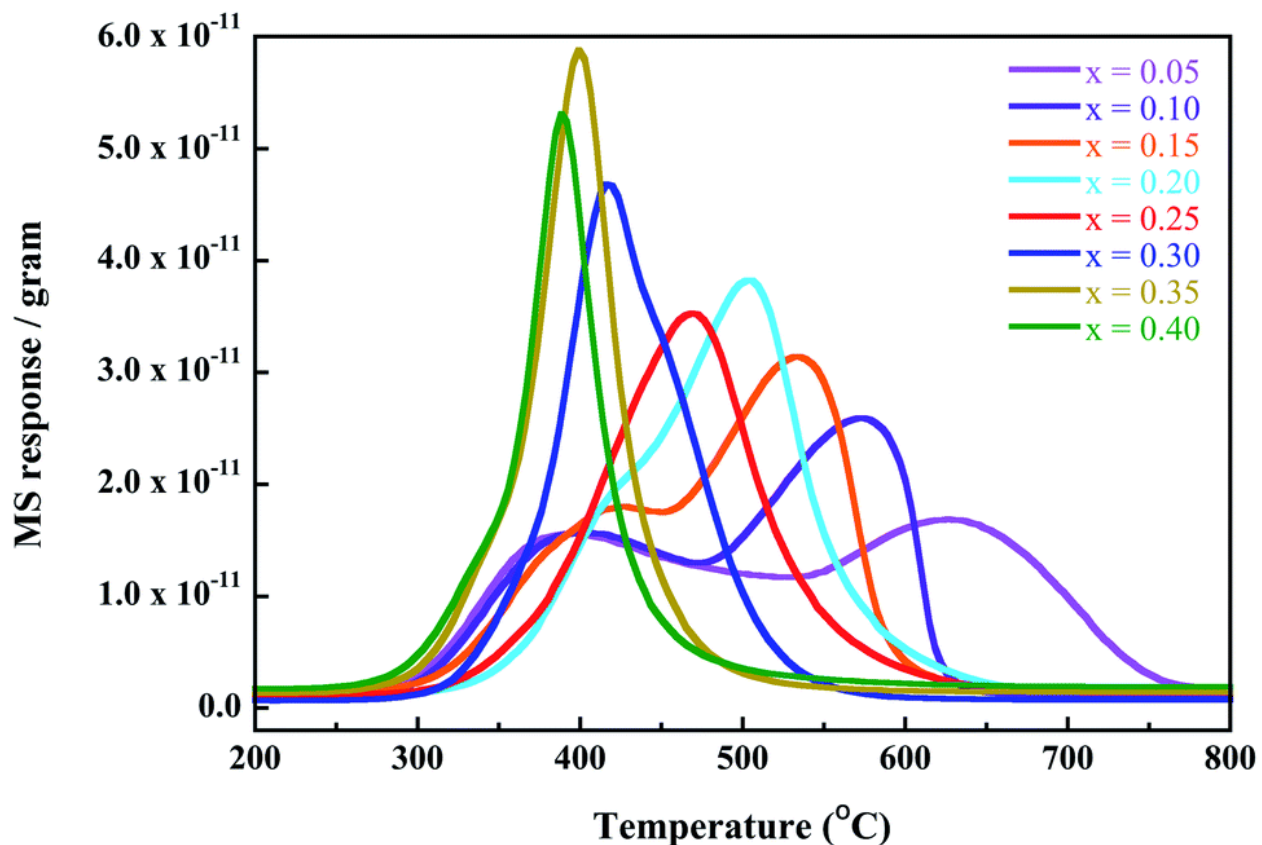


Fig. 5 Displays the O_2 -TPD traces (m/z 32) for the $\text{Sr}_{1-x}\text{Ca}_x\text{FeO}_{3-\delta}$ samples under He flow prior to the desorption sweep, the samples are heated to $800\text{ }^{\circ}\text{C}$ in air, allowing for an increased uptake of oxygen, followed by rapid cooling. The shift in the desorption maximum is highly notable as it trends with the amount of Ca added to the SrFeO_3 lattice.

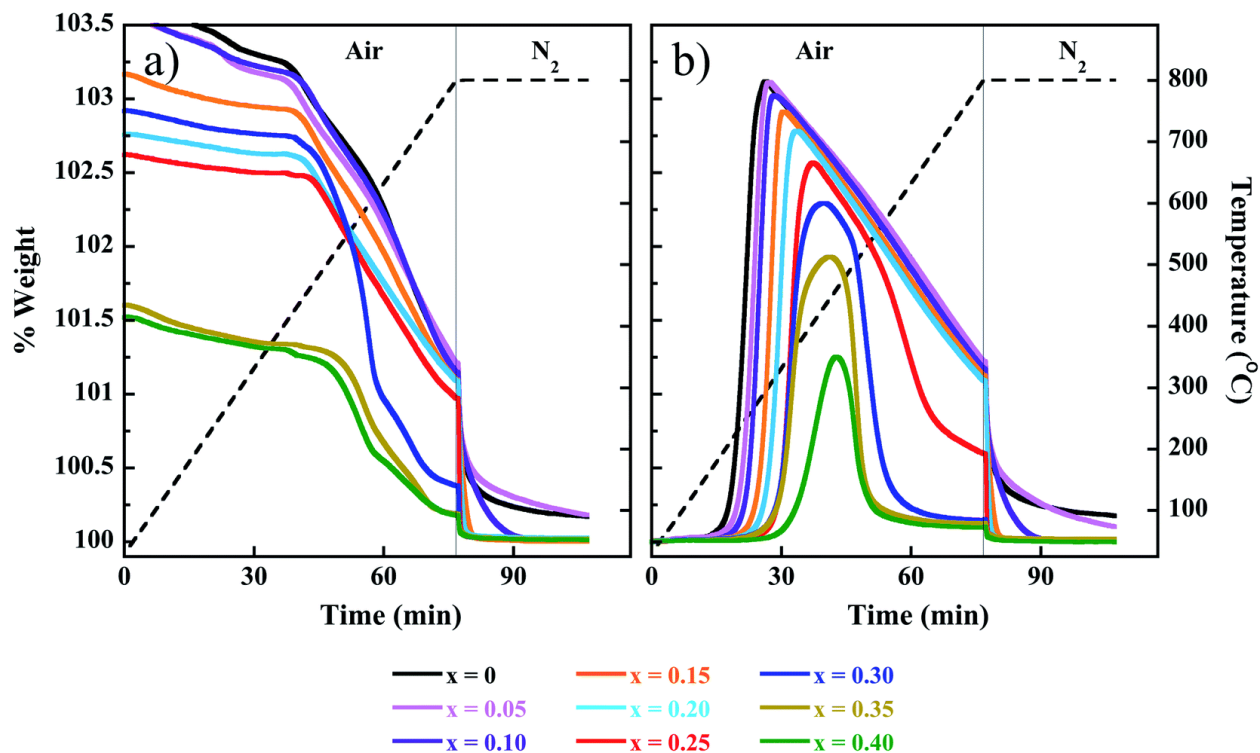


Fig. 6 Displays TGA curves for the $\text{Sr}_{1-x}\text{Ca}_x\text{FeO}_3$ series gathered by heating the samples in air to 800 $^\circ\text{C}$, followed by switching to N_2 flow. (a) The first run was performed rapidly (10°min^{-1} from 30–800 $^\circ\text{C}$) whereas the re-oxidation feature in (b) was analyzed immediately following cooling in N_2 flow.

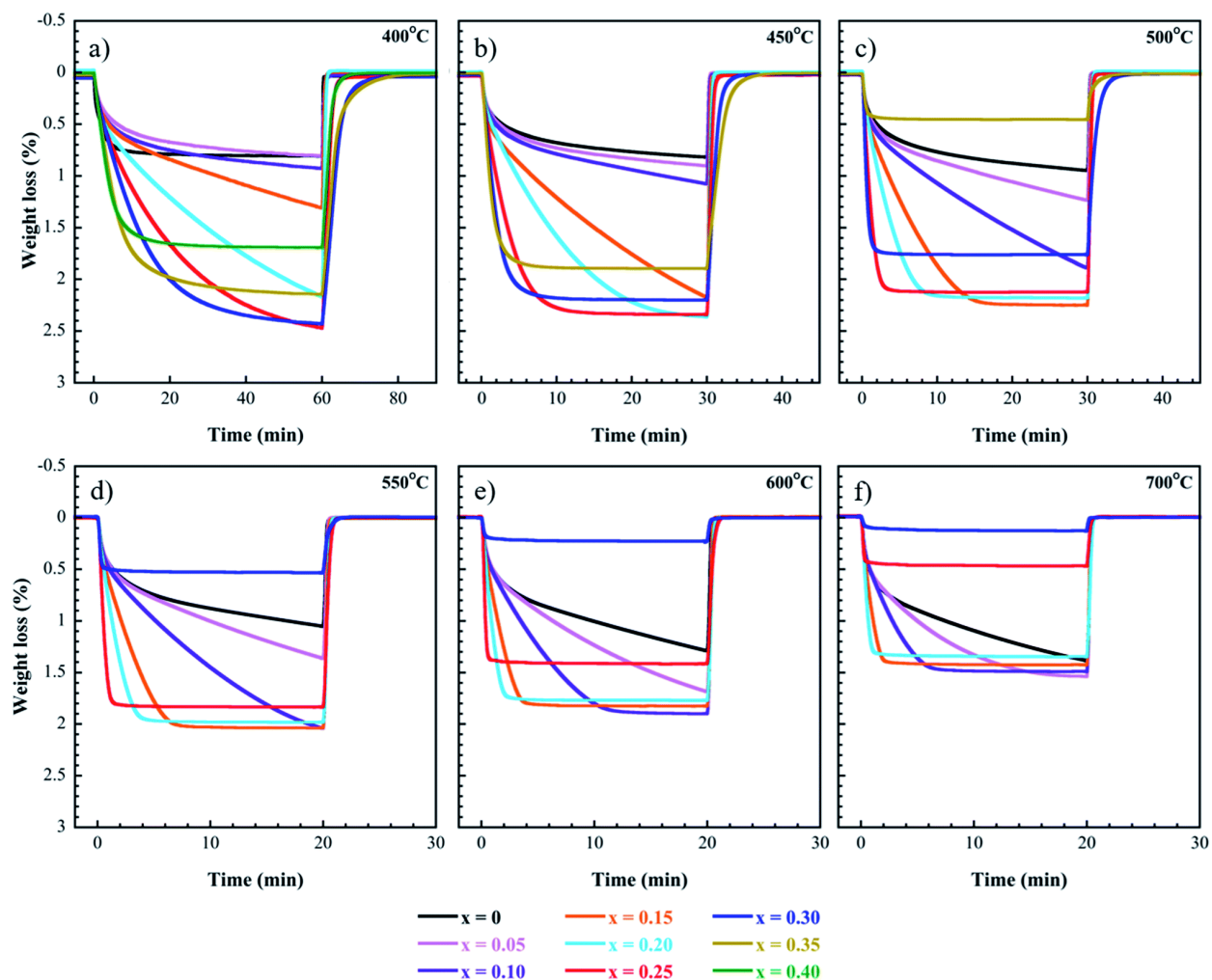


Fig. 7 Shows the second isothermal TGA oxidation/reduction curves for the $\text{Sr}_{1-x}\text{Ca}_x\text{FeO}_{3-\delta}$ series at temperatures of (a) 400 °C; (b) 450 °C; (c) 500 °C; (d) 550 °C; (e) 600 °C; and (f) 700 °C. The oxidation gas stream is 75 sccm air and the reduction gas stream is 75 sccm N_2 . 0% weight loss represents the weight% of the reversibly-accessed oxidized species.

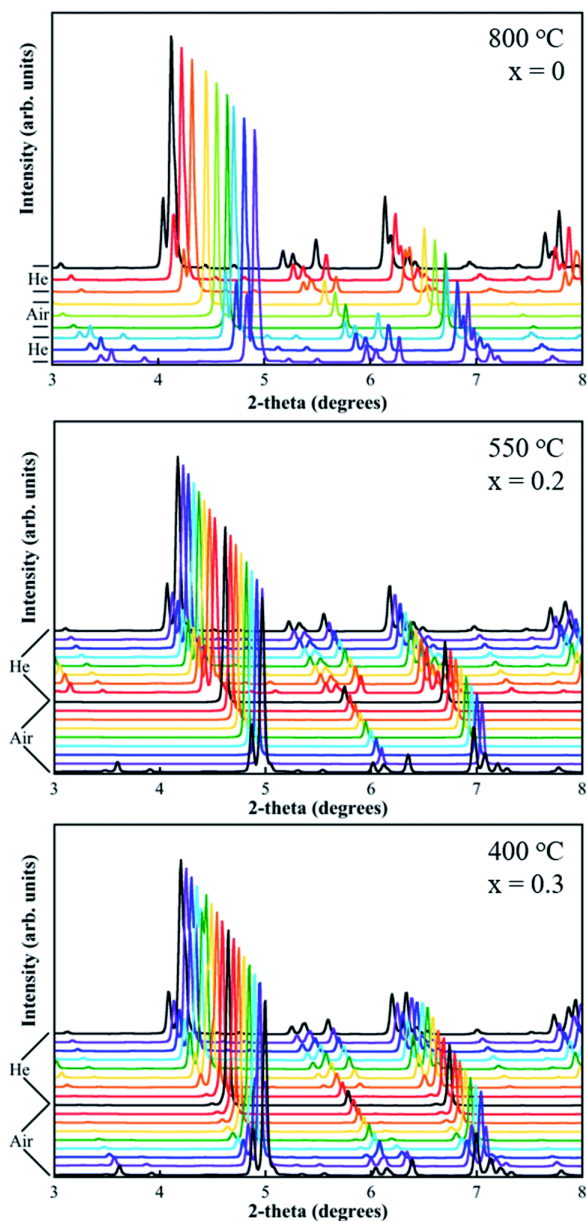


Fig. 8 Contains in situ synchrotron powder X-ray diffraction patterns during air/He cycling. (top) SrFeO₃ at 800 °C, 1 min resolution. (middle) Sr_{0.8}Ca_{0.2}FeO₃ at 550 °C, 2 min resolution. (bottom) Sr_{0.7}Ca_{0.3}FeO₃ at 400 °C, 3 min resolution. Black scans signify gas changes in the middle and bottom figures.